Discrete simulations of fluid-driven transport of naturally shaped sediment particles

Qiong Zhang[1], Eric Deal[2,3], J. Taylor Perron[2], Jeremy G. Venditti[4], Santiago J. Benavides[2,5], Matthew Rushlow[2], Ken Kamrin[1]

[1]Department of Mechanical Engineering, Massachusetts Institute of Technology, Cambridge, Massachusetts, USA
[2]Department of Earth, Atmospheric, and Planetary Sciences, Massachusetts Institute of Technology, Cambridge, Massachusetts, USA
[3]Now at Department of Earth Sciences, Engineering Geology, ETH Zurich, Zurich, Switzerland
[4]Department of Geography, Simon Fraser University, Burnaby, British Columbia, Canada
[5]Now at Mathematics Institute, University of Warwick, Coventry, UK

Key Points:

- A novel numerical method is developed for bedload transport of naturally shaped particles, using hundreds of distinct shapes from scanning.
- Benchmarked by flume experiments, the simulations further validate a recent sediment transport relation for aspherical grain shapes.
- Particles below the bed surface tend to align with the flow direction, but this tendency reduces moving from the dense to dilute regions.

Corresponding author: Ken Kamrin, kkamrin@mit.edu

Abstract

A numerical scheme is developed to simulate the transport of natural gravel. Starting with computerized tomographic (CT) scans of natural grains, our method approximates the shapes of these grains by "gluing" spheres of different sizes together with overlaps. The conglomerated spheres move using a Discrete Element Method (DEM) which is coupled with a Lattice Boltzmann Method (LBM) fluid solver, forming the first complete workflow from particle shape measurement to high resolution simulations with hundreds of distinct shapes. The simulations are quantitatively benchmarked by flume experiments. The numerical tool is used to further validate a recently proposed modified sediment transport relation, which takes particle shape effects into account, including the competition between hydrodynamic drag and material friction. Unlike a physical experiment, our simulations allow us to vary the hydrodynamic drag coefficient of the natural gravel independently of the material friction. Our studies support the modified sediment transport relation. The simulations also provide insights on the particle-level kinematics, such as particle orientations, in the bedload transport process. Particles below the bed surface prefer to orient with their shortest axes perpendicular to the bed surface, but the tendency goes down as the packing fraction decreases far from the bed surface. The particles rotate freely in the dilute particle flow regime.

Plain Language Summary

When simulating the bedload transport of aspherical sediment particles, it is challenging to have a realistic representation of the particle shape and size distributions. Here, we develop a novel numerical scheme to simulate the transport of naturally shaped sediment particles. The particle shapes are constructed using multiple overlapping constituent spheres to approximate the shapes of real river gravel. This is the first complete workflow that measures actual particle shapes and simulates the transport of hundreds distinct realistic grains. Agreement with flume experiments is observed. With the benchmark in hand, a recently proposed sediment transport relation for systems of many particle shapes is validated by varying the hydrodynamic drag coefficient independently in the simulations. The high resolution simulations are also used to study the particle-level behaviors. The preference of particle orientations decreases going from dense to dilute regions.

1 Background

When fluid flows above a sediment bed, particles slide, roll and saltate along the bed surface. This is known as bedload transport, which plays important roles in the shaping of natural landscapes and the engineering of artificial hydraulic structures. In bedload transport, sediment particle shapes have been long considered to have a strong influence on the channel-scale behavior of sediment transport, including the relation between sediment flux and bed shear stress (Shields, 1936; Ferguson & Wathen, 1998; Warburton & Demir, 2000; Demir, 2000; Dudill et al., 2020; Jain et al., 2021; Deal et al., 2023), as well as the threshold shear stress required for transport (Komar & Li, 1986; Yager et al., 2018; Jain et al., 2021). The macroscopic outcomes originate from the shapes' effect on particle dynamics, affecting the resulting packing fraction (Donev et al., 2004), orientation (Eshghinejadfard et al., 2018), permeability (Blois et al., 2014), modes of particle motion (Allen, 2012), drag reduction (Ardekani et al., 2017), and fluidization (Zhou et al., 2011). These particle scale kinematics and dynamics require detailed measurements of the particle motion (translational and rotational), forces, and torques, which are not easily accessible in physical experiments. DEM based coupled simulations (with fluid) resolve the individual particles, and therefore can serve as a complementary approach to study the bedload sediment transport of aspherical particles from a microscopic perspective. Beyond giving access to detailed grain and fluid information, numerical sim-

Table 1: Recent discrete simulations of the sediment transport of aspherical particles.

Numerical studies	Shape	Fluid	Coupling	Shapes per run
Schmeeckle, 2014	Spheres	LES	Empirical drag law	1
Bravo et al., 2018	Ellipsoids	Imposed	Analytical drag law	1
Zhang et al., 2020	Ellipsoids	LES	Interfaces resolved	1
Jain et al., 2021	Ellipsoids	DNS	Interfaces resolved	1
Sun et al., 2017	Bonded-spheres	LES	Empirical drag law	1
Alihosseini & Thamsen, 2018	Multi-spheres	RNG $k-\varepsilon$	Empirical drag law	1
Shao et al., 2019	Multi-spheres	$k-\varepsilon$	Empirical drag law	1
Fukuda & Fukuoka, 2019	Multi-spheres	LES	Interfaces resolved	1
Fukuoka et al., 2014	Multi-spheres	LES	Interfaces resolved	4
This work	Multi-spheres	LES	Interfaces resolved	669

ulations can perform virtual experiments for conditions that are difficult to achieve in the lab (e.g. complex geometries, periodic boundaries, or a different gravitational environment).

Discrete simulations of sediment transport of aspherical particles are challenging in terms of the representation of the particles and the coupling between the fluid and the moving particles. Existing numerical methods differ in the way these two problems are handled. An overview of numerical techniques in recent studies of aspherical sediment transport are listed in Table 1. See Zhong et al. (2016) for earlier research.

The coupling between the fluid and moving particles is mainly determined by how the fluid is represented. One can simply impose a fluid velocity field that is not affected by the grains, such as Bravo et al. (2018), leading to a one-way coupling. Most commonly, the fluid phase is instead solved on meshes using the finite volume method (FVM) or the finite element method (FEM) with a turbulent closure (such as large eddy simulations, LES) or, with enough resolution, even a direct numerical simulation (DNS). The length-scale at which the fluid is resolved determines the way the fluid-particle interaction is handled. When the grid size is greater than or comparable to the particle size, the momentum exchange is estimated using analytical or empirical drag laws based on the homogenized solid fields (such as packing fraction and velocity). When the grid size is much smaller than the particle size, the interface can be resolved and the momentum exchange on individual particles can be integrated more accurately. This work adopts an LES fluid solver with sub-particle resolution to resolve the moving interfaces of the particles.

Discrete simulations for the particle motion are all based on DEM, in which the particles are individually tracked. The early work (Schmeeckle, 2014) used an empirical drag law for irregular sand particles, though the solid phase was still represented by spheres. Ellipsoids (Bravo et al., 2018; B. Zhang et al., 2020; Jain et al., 2021) are one of the easiest representations of aspherical shapes. In terms of the particle shape representation method, besides the single-particle representation, the clustered-particle approach in which the particle shape is approximated by a cluster of spheres, has gained increasing usage in recent years. Sun et al. (2017) bonded spheres together (no overlaps) to represent geometrically rough particles, but the shapes are not commonly seen in nature due to the large indentations between neighboring spheres. Another type of clustered-particle approach – the multi-sphere technique, which uses overlapping spheres to approximate aspherical shapes – was first introduced for dry particle simulations (Favier

et al., 1999, 2001). It was later adopted in numerical studies of sediment transport (Alihosseini & Thamsen, 2018; Shao et al., 2019; Fukuoka et al., 2014; Fukuda & Fukuoka, 2019). It is worth noting that most of the previous numerical studies use multi-sphere particles of a single shape in each simulation, lacking a real representation of particle size and shape distributions. Only Fukuoka et al. (2014) used multiple (four) distinct realistic shapes in a single simulation. As more accurate algorithms to approximate real particles using the multi-sphere method have been developed (Amberger et al., 2012; Li et al., 2015), simulating the sediment transport of realistic naturally shaped particles has been made possible to better understand the microscopic physics and the development of more accurate sediment transport relations. Our work here utilizes the overlapping multi-sphere approach.

Our numerical method will allow us to simulate the most realistic numerical flume experiment of natural grains to date. With this tool, we hope to confirm recent results regarding the effect of grain shape on sediment transport. In terms of the quantification of grain shape effects in sediment transport, recent experiments (Deal et al., 2023) have shown that shape effects can be quantified as a competition between the hydrodynamic drag (driving factor) and the resistance of the material due to bulk friction. The sediment volume flux per unit flow q_s is nondimensionalized into q^*, the dimensionless sediment transport rate (the Einstein number):

$$q^* \equiv q_s \Big/ \left(d_p \sqrt{\frac{\rho_s - \rho_f}{\rho_f} g d_p} \right), \tag{1}$$

with d_p the grain diameter, g the gravitational acceleration, and ρ_s and ρ_f the sediment and fluid densities. In the most commonly used sediment transport relation (Meyer-Peter & Müller, 1948), q^* is usually expressed as a 3/2 power-law of the bed shear stress τ_b with a threshold. τ_b is nondimensionalized into the dimensionless bed shear stress τ^*, often referred to as the Shields number:

$$\tau^* \equiv \tau_b \big/ \left[(\rho_s - \rho_f)\, g d_p \right]. \tag{2}$$

To incorporate grain shape effects into the transport relation, Deal et al. (2023) introduced two more quantities. On one hand, irregular shapes increase the hydrodynamic drag coefficient, which in return helps the particles transport with the flow. Correspondingly, the first quantity is C^*, the ratio of the effective drag coefficient C_D to the drag coefficient of the volume-equivalent sphere C_o:

$$C^* = \frac{C_D}{C_o} = \frac{C_{D_{\text{settle}}} S_f}{C_o}. \tag{3}$$

C_D is calculated as the product of the drag coefficient of the particles settling in still water, $C_{D_{\text{settle}}}$, and the Corey shape factor S_f (Corey, 1949), which accounts for the fact that the orientation of the settling particle in still water prefers the largest drag while the orientation of the transported sediment particle is always changing due to tumbling. On the other hand, irregular shapes make the particles experience larger resistance when moving along the bed surface. This is accounted for by μ^*:

$$\mu^* = \frac{\mu_s - S}{\mu_o - S}, \tag{4}$$

which is the average bulk friction coefficient μ_s normalized by the bulk friction coefficient of spheres μ_o, both modified by the influence of the bed surface slope S. Based on a physical derivation and confirmed in experiments, Deal et al. (2023) have found that the dimensionless sediment transport relation of particles of arbitrary shapes is collapsed when parameterized by C^*/μ^*:

$$q^* = \alpha_o \left(\frac{C^*}{\mu^*} \tau^* - \tau^*_{co} \right)^{3/2}, \tag{5}$$

where α_o and τ^*_{co} are the transport coefficient and threshold of motion for idealized spheres. The newly proposed transport relation Eq 5 has been tested on 5 different particle shapes in flume experiments, from spheres to naturally shaped particles. However, the physical experiments can not independently vary the two key factors (repose angle and drag coefficient). Also, some output variables such as the forces and the orientations of the particles cannot be easily measured in the experiments. These well controlled experiments provide ideal benchmark cases for numerical simulations, which in turn can be used to check the robustness of Eq 5 by independently controlling or varying the factors and to understand the microscopic kinematics.

This work is dedicated to developing a novel fully-coupled discrete particle-fluid simulation methodology for the study of particle shape effects in bedload sediment transport processes, which is the first implementation of DEM-LBM based on the multi-sphere approach and the first complete workflow from shape measurements and approximation to the coupled simulations of many differing aspherical particles in fluid. Compared with previous numerical approaches, this work offers several advantages. First, we used the most recent multi-sphere approximation algorithm to produce more accurate shape representations. Second, many distinct realistic natural gravel shapes (more than 600 shapes) from CT scanning were represented in each simulation, permitting realistic size and shape distributions. Third, the numerical method was closely benchmarked with corresponding flume experiments. After benchmarking the numerical method quantitatively with the corresponding experiments, we used simulations for further validation of the recently proposed sediment transport relation (Deal et al., 2023). While it is not easy to change the drag coefficient and the repose angle of the sediment particles independently in physical experiments, the numerical tool allows us to set up simulations varying the drag coefficient independently. Regarding the modified transport relation's assumption that the particle orientations while being transported is different from the orientations while settling in still water, particle orientations as well as other particle-level kinematics were also studied in simulations for a more complete physical picture of the entire bedload transport process.

2 Numerical method: multi-sphere technique

2.1 Multi-sphere approximation of natural gravel shapes

Rushlow (2020) reconstructed the natural gravel particles used in the experiments (Deal et al., 2023), based on CT scans provided by the microCT Lab in University of Minnesota. Based on the scanning results, a greedy heuristic algorithm was employed to superimpose a set of overlapping spheres, which is adapted from the algorithm proposed by Li et al. (2015). After uniformly discretizing the scanning result into a fine voxelation of cells, a sphere is inserted fully inside the shape such that the sphere encompasses the most number of cells. When a new sphere is required to be inserted, the sphere that adds the most number of cells into the occupied volume is selected. This repeats until the desired number of spheres have been inserted for the shape approximation.

Figure 1 from Rushlow (2020) shows the comparison between the original scanned result and the approximations using different numbers of component spheres. A cluster of 20 component spheres can capture the shape of the natural particles fairly well, without creating too much overfitting near the thin edges. In the current work, the shape of each particle is approximated using 20 constituent spheres. More detailed descriptions of the CT scanning, the shape approximation procedures, and the quantification can be found in Rushlow (2020). Since the sphere insertion process under-represents the volume on its own, about 85% of the total volume is on average represented. Note that the volume of the multi-sphere particle is determined by counting the number of cells encompassed in the envelope, so the overlaps are not double counted. The actual repre-

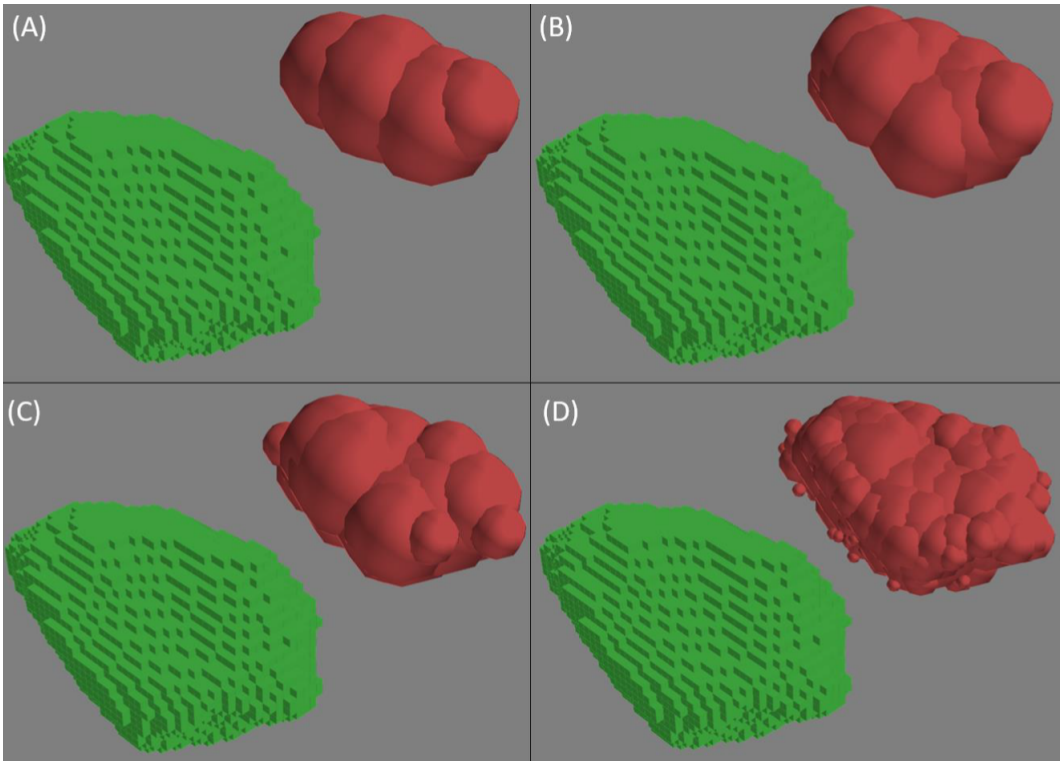

Figure 1: Multi-sphere approximation using different numbers of spheres (green: the original natural grain voxelated from CT scanning; red: the multi-sphere approximation). (A) 5 sphere approximation. (B) 10 sphere approximation. (C) 20 sphere approximation. (D) 150 sphere approximation. Figure reproduced from Rushlow (2020).

sented volume is used for the calculation of the volume equivalent diameter d_o. As a result, the d_o values in the simulations are slightly ($\sim 5\%$) smaller than the experiments.

2.2 Coupled DEM-LBM scheme

Our previous numerical work (Q. Zhang et al., 2022) for round particles, which was validated against corresponding flume experiments, showed that the coupled DEM-LBM approach has the capability to resolve sub-particle scale physics in the bedload sediment transport of spherical particles. In this work, we modified the DEM-LBM coupling scheme of spherical particles for multi-sphere particles to include proper rigid-body constraints within each multi-sphere cluster (see Figure S1 in the Supporting information for the flow chart of the numerical scheme).

The position and velocity of the spheres within each grain are used to update the grain's solid domain as seen by the fluid. Then fluid-solid momentum transfer is dealt with in the same way (Bouzidi et al., 2001) as the DEM-LBM for spherical particles as long as a fluid-solid interface has been detected. Then, instead of passing the (linear and angular) momentum transfer back to the spheres, they are integrated on each multi-sphere grain shape. Similar to the original DEM-LBM scheme, the hydrodynamic forces (and torques) on each shape in the current and the previous LBM steps are averaged when conducting the DEM update, to reduce numerical oscillations. In a DEM step, the particle-particle contacts are calculated by considering the contacts of the constituent spheres within different particles. By summing these two contributions of momentum transfer

and the buoyancy force, the linear and angular acceleration of each shape can be obtained, which is required in the Velocity Verlet method (Swope et al., 1982) for the update of the velocity and rotational velocity of the shape. Then in each rigid body (shape) the constituent spheres must move as a rigid object. Thus the velocity of each component sphere is updated according to the velocity of the shape as well as the cross product of the angular velocity of the shape and the position of the sphere relative to the centroid of the shape (Fukuoka et al., 2014). Note that the acceleration of each sphere also needs to be obtained, which will be used for the update of position and velocity in the middle of the time step. Special care should be taken regarding the linear acceleration originating from the rotation of the shape, which can be seen as a constraint to satisfy rigid body assumptions.

2.3 Repose angle and settling velocity

Before setting up flume simulations for the comparison of the sediment transport relation with the experiments, the material properties of the actual particles sampled from the river bed need to be benchmarked. The naturally shaped particles have an average density of $\rho_s = 2471\,\mathrm{kg/m^3}$. The diameter of the volume equivalent sphere is $d_o = 4.1\,\mathrm{mm}$. The average settling velocity is $w_s = 0.286\,\mathrm{m\,s^{-1}}$ whereas the settling velocity of the volume equivalent sphere is $w_o = 0.436\,\mathrm{m\,s^{-1}}$, corresponding to drag coefficients $C_{D_{\mathrm{settle}}} = 0.67$ and $C_o = 0.42$. The repose angle of the dry material is 38°. Methods used to measure these properties are described in Deal et al. (2023).

The previous subsection described how the shapes of the multi-sphere particles are matched with the scanned naturally shaped particles. Besides that, the Corey shape factor S_f (relative flatness) of the multi-spheres, measured to be 0.67 on average, exactly matches that measured from the voxelated scanning results, confirming that the multi-sphere approximation using 20 constituent spheres can capture the natural shapes well. The diameter of the volume equivalent sphere of the multi-sphere particles is 3.9 mm, which is used in the calculation of the drag coefficient. This value is slightly ($\sim 5\%$) smaller than the measurement in the experiments, as mentioned in the previous section.

Here we check other important particle properties in Eq 5, including the repose angle of the dry material and the average settling velocity in still water. The repose angle test was carried out by simulating pouring the multi-sphere particles onto a rough table. Both the particle-particle and wall-particle friction coefficients were set to 0.8 (measured to be 0.78±0.04 in experiments). Figure 2(a) shows a snapshot of the pile of multi-sphere particles. The radial locations of the constituent spheres are plotted with their vertical positions in Figure 2(b). The repose angle in the simulation is measured as 37°, close to the 38° repose angle measured in the experiments. After pouring down nearly 1800 particles, the pile ended up with a similar size to that of the experiments (see Figure 2, the 37° slope approximately ends at a radius of 6cm).

For DEM-LBM simulations of round particles, Feng and Michaelides (2009) and Derksen (2014) have shown that guaranteeing the fluid grid size $dx \leq d_o/6$ or $dx \leq d_o/8$ was adequate for sufficiently accurate fluid coupling. In our previous work (Q. Zhang et al., 2022), dx was kept to be smaller than 1/10 of the radius of the spherical particles to guarantee enough accuracy. In this work with different particle shapes and a different average size, we kept $dx \leq d_o/8$ by always choosing the grid size to be $dx = dx_0 \equiv 0.5\,\mathrm{mm}$. Even so, with this choice, the diameter of the smallest constituent sphere is comparable to the grid size in the LBM mesh ($\sim 0.9dx_0$). It is not clear how resolved each constituent sphere must be on the LBM mesh for accuracy with multi-sphere particles. Settling simulations in still water were set up in a 3 cm by 3 cm by 18 cm domain (periodic boundary condition for the side walls and no-slip boundary condition for the top and bottom) with a randomly chosen set of 34 multi-sphere particles. The number of tested particles is limited due to the high computational cost of the simulations with a reso-

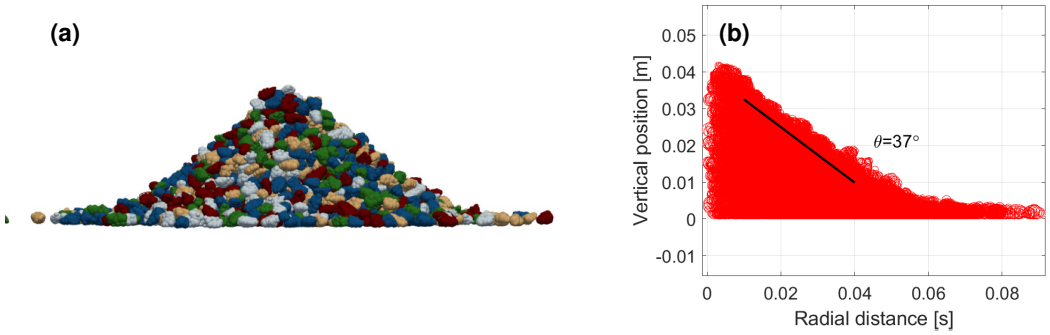

Figure 2: Repose angle simulation of the multi-sphere particles. In total, nearly 1800 particles in 627 distinct shapes are used (none used more than 3 times). (a) Snapshot of the simulation result after pouring. (b) Vertical positions of particles plotted against their radial distance from the vertical center line. The multi-sphere particles show a 37° repose angle.

Table 2: The average settling velocities on the same set of 34 multi-sphere particles with different resolutions.

	dx_0	$dx_0/2$	$dx_0/5$	Experiments
Settling velocity [m/s]	0.254	0.276	0.280	0.286

lution of $dx_0/5$. The average settling velocities with different resolutions are shown in Table 2. The experiments (Deal et al., 2023) measured the average settling velocity on a set of 23 particles which were not identical to the set of 34 particles tested in the simulations, so the average settling velocity of these two sets may be slightly different. Even so, the results do show convergence as the grid size decreases from dx_0 to $dx_0/5$. When dx_0 is halved, the settling velocity increases by 9.2%. But as the grid size shrinks a further 2.5 times, the settling velocity is only changed by 1.5% and the value is close to that measured in the experiments (slower by 3.5%). Increasing the whole domain size will also help reduce the hindrance effect due to the side boundaries and would make the result closer to the experimental measurement.

Although the settling results would suggest that our choice of having a resolution of dx_0 is under-resolving the grains, halving the current grid size by a factor of 2 means the number of fluid nodes in all 3 dimensions are increased by a factor of 2. This also requires a halved fluid timestep, which multiplies the total computational cost on the fluid side by a factor of 16. The question is if there is an alternative way to match the settling velocity in still water while keeping "a coarser" grid size. A workaround we have identified is to shrink the size of the constituent spheres universally when viewed by the LBM solver (not in the DEM solver) without shifting the placement of their centers. This way, the cross-section of the grains in the flow are smaller, countering the effect that particles usually look bigger on the fluid nodes than their actual size due to discretization effects on the LBM grid. The amount that the constituent spheres' radii are universally decreased by can be normalized by dx into a dimensionless factor Sk, the shrinkage coefficient. See Figure S2 in the Supporting Information for an illustration of the particle representation on the solid and fluid solvers as Sk changes. The average settling velocities and the corresponding C^* values on a set of 480 multi-sphere particles with different shrinkage coefficients are shown in Table 3. As Sk increases, the average settling ve-

Table 3: The average settling velocities and drag coefficients on a set of 480 multi-sphere particles with different shrinkage coefficients (resolution: dx_0).

	$Sk = 0.00$	$Sk = 0.55$	$Sk = 0.70$
Settling velocity [m/s]	0.246	0.273	0.286
C^*	1.92	1.55	1.41

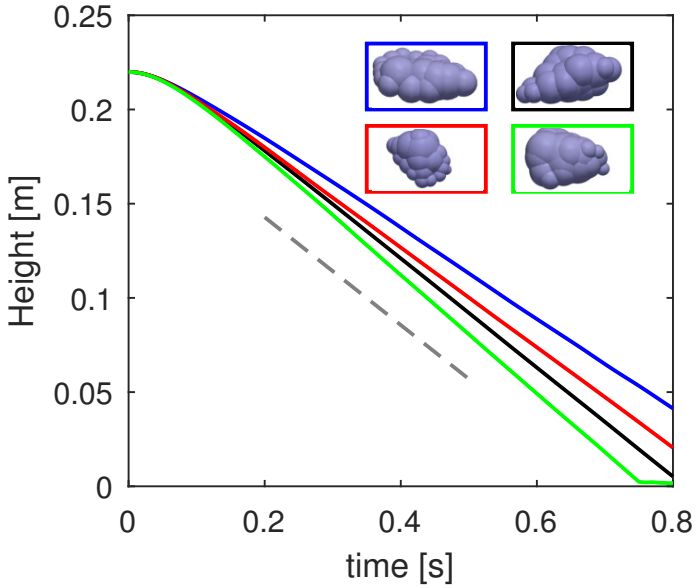

Figure 3: Height as a function of time when 4 example simulated particles ($Sk = 0.70$) settle in water at moderate Reynolds numbers ($900 \sim 1700$). The shapes of the settling particles are shown in the inset figures whose box colors match the curve colors. The dashed grey line corresponds to the average settling velocity ($0.286\,\mathrm{m\,s^{-1}}$) on a set of 480 simulated particles.

locity increases and the rate of the increase also increases with Sk. $Sk = 0.70$ gives the same average settling velocity of $0.286\,\mathrm{m\,s^{-1}}$ as that measured in the experiments. Figure 3 shows the height as a function of time on four exemplary settling particles with $Sk = 0.70$. See Movie S1 in the Supporting Information for the detailed particle motion in this process. The particles tend to expose their largest cross-sectional area as they settle.

Note that Sk only shrinks the size of the constituent spheres as seen by the fluid, leaving the solid phase properties (size, mass, interactions, etc.) unchanged. The buoyant force on each particle is calculated analytically from the volume of the multi-sphere shape seen by the DEM, which is not influenced by Sk either. One potential concern is whether the amount of shrinkage used opens up gaps in the compound grains, which are large enough to allow fluid to flow through. Actually, only in rare cases do gaps form, and the width is typically smaller than $0.3dx_0$ with a very low chance to be resolved by the mesh. See Text S1 in the Supporting Information for more details. This shrinkage workaround also provides an opportunity to vary the drag coefficient independently of other grain properties, without changing any other key factors in Eq 5.

3 Simulations and results

3.1 Comparison with laboratory flume experiments

Physical experiments for naturally shaped gravel particles in a narrow flume were described in Deal et al. (2023) and Benavides et al. (2022). In each experiment, naturally shaped particles and water were fed into the inclined flume from the upstream end at a given combination of volume flux rates. After the initial period of sediment deposition, the granular bed built up and steady state was reached. Then the slope of the free water surface S as well as the water depth were measured, and the particle motion was recorded by a high-speed cameras in the middle section of the flume, which was 10.2mm wide.

The simulated virtual domain has a length $L = 0.12\,\mathrm{m}$ and height of $0.15\,\mathrm{m}$ (bed thickness is approximately $0.05\,\mathrm{m}$). The LBM lattice has homogeneous grid size $dx_0 = 0.5\,\mathrm{mm}$. The first and last nodes across the flume align with the side walls, and the simulated flume width is $W = 10.5\,\mathrm{mm}$ (22 nodes across the flume). The top of the simulated domain uses a free-slip (zero gradient) boundary condition. Note that in this narrow flume configuration, the fluid velocity far above the granular bed surface approaches a constant value due to sidewall shear. The bottom uses a no-slip boundary condition and the two sides perpendicular to the flow direction are connected with periodic boundary conditions. For the two side walls of the flume, a Navier-type boundary condition (Q. Zhang et al., 2022) is used to account for the fluid velocity jump across the near-wall boundary layer. The gravity $g = 9.8\,\mathrm{m/s^2}$ is applied at an angle of slope S with respect to the vertical axis of the simulated domain. The flow is driven by the horizontal component of the tilted gravity vector. Inside the flume, there are 1000 multi-sphere particles of 627 distinct shapes (each shape used at most twice). The elastic constants for the normal and tangential contacts are set to be $2000\,\mathrm{N\,m^{-1}}$ and $571.4\,\mathrm{N\,m^{-1}}$, respectively, guaranteeing the constituent spheres are in the hard limit. The damping coefficient of the particles is $0.03\,\mathrm{kg\,s^{-1}}$.

The DEM-LBM flume simulations use the calibrated multi-sphere particles with $Sk = 0.70$, which produces the same average settling velocity as the experiments. The initial condition sets the particles uniformly distributed throughout the whole domain with no velocity and with stationary fluid. As each simulation runs, gravity drives the fluid and grains, resulting in the ultimate formation of a particle sediment bed and a transverse fluid flow profile, which transports the near-surface particles. The simulation results are similar to the experiments in terms of bed surface structure and the collective behaviors of the transported particles, as shown in Figure 4 for two different Shields numbers. See Movie S2 in the Supporting Information for a side-by-side video comparison of the simulations and experiments.

For quantitative comparisons, the simulations were all carried out for 40 s of simulation time and the last 30 s of the simulations were taken to calculate the time averaged integrated flux. For the calculation of q^*, the sediment volume flux per unit width q_s is counted in the whole domain as

$$q_s = \frac{\Sigma_i \mathrm{Vol}_i V_{i,x}}{LW}, \tag{6}$$

where $V_{i,x}$ and Vol_i are the streamwise velocity and the volume of the i-th particle (volume of the multi-sphere shape, not influenced by the shrinkage coefficient Sk), respectively. For the calculation of τ^*, the bed shear stress τ_b is calculated as

$$\tau_b = 2.41 \rho_f g S \frac{HW}{2H + W}, \tag{7}$$

where H is the water depth measured down to the bed surface, W is the flume width, $\frac{HW}{2H+W}$ is the hydraulic radius, and the factor of 2.41 corrects for wall effects (Deal et al.,

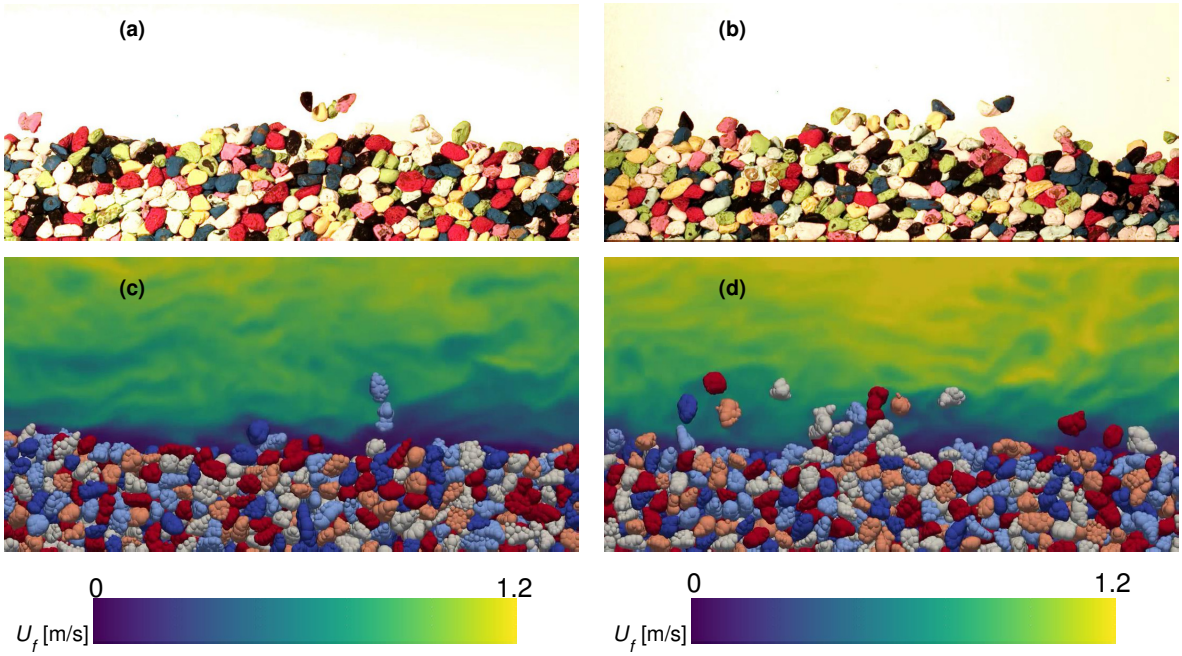

Figure 4: Comparisons between the flume experiments and DEM-LBM simulations of multi-sphere particles at Shields number $\tau^* = 0.113$ (left column) and $\tau^* = 0.147$ (right column). (a) & (b): Snapshots of the flume experiments. (c) & (d): Snapshots of the DEM-LBM simulations of the multi-sphere particles with fluid field colored by the fluid velocity magnitude on the center-plane of the flume.

2023). Note there are also other methods to estimate τ_b, such as the method in our previous numerical work on spherical particles (Q. Zhang et al., 2022) as well as the work based on the same experiments (Benavides et al., 2022). More details about different methods of estimating the boundary shear stress can be found in Deal et al. (2023). The resulting transport relation compared with the experimental results is shown in Figure 5(a).

Overall, in terms of the q^* vs τ^* transport relation, the DEM-LBM simulations are consistent with the experiments. From a statistical perspective, the threshold τ_c^* for the naturally shaped particles in Benavides et al. (2022) is 0.096 ± 0.019, near which the simulations' results may not be performed long enough for representative average values due to strong intermittency. For the other data points at medium to high transport stages, the values of dimensionless transport rate, q^*, from the simulations and the experiments match well for natural gravel, giving results far below the transport relation obtained from glass spheres. Figure 5(b) shows the data when the horizontal axis is modified from τ^* into $\tau^* C^*/\mu^*$, following Eq 5 as proposed recently in Deal et al. (2023). The numerical results of the multi-sphere particles, (glass) spheres, as well as the corresponding experimental results collapse onto the same master curve upon rescaling.

3.2 Parameter study: effect of drag coefficient

Recall that changing the shrinkage coefficient Sk only changes the average settling velocity without influencing the other key factors purely dependent on the DEM: the diameter of the volume-equivalent sphere and the repose angle of the dry material. As mentioned previously, tuning Sk varies the settling velocity (the drag coefficient) independently, providing an opportunity to probe the parameter space as a further check of Eq 5. Two sets of DEM-LBM simulations with the same set of 1000 multi-sphere particles

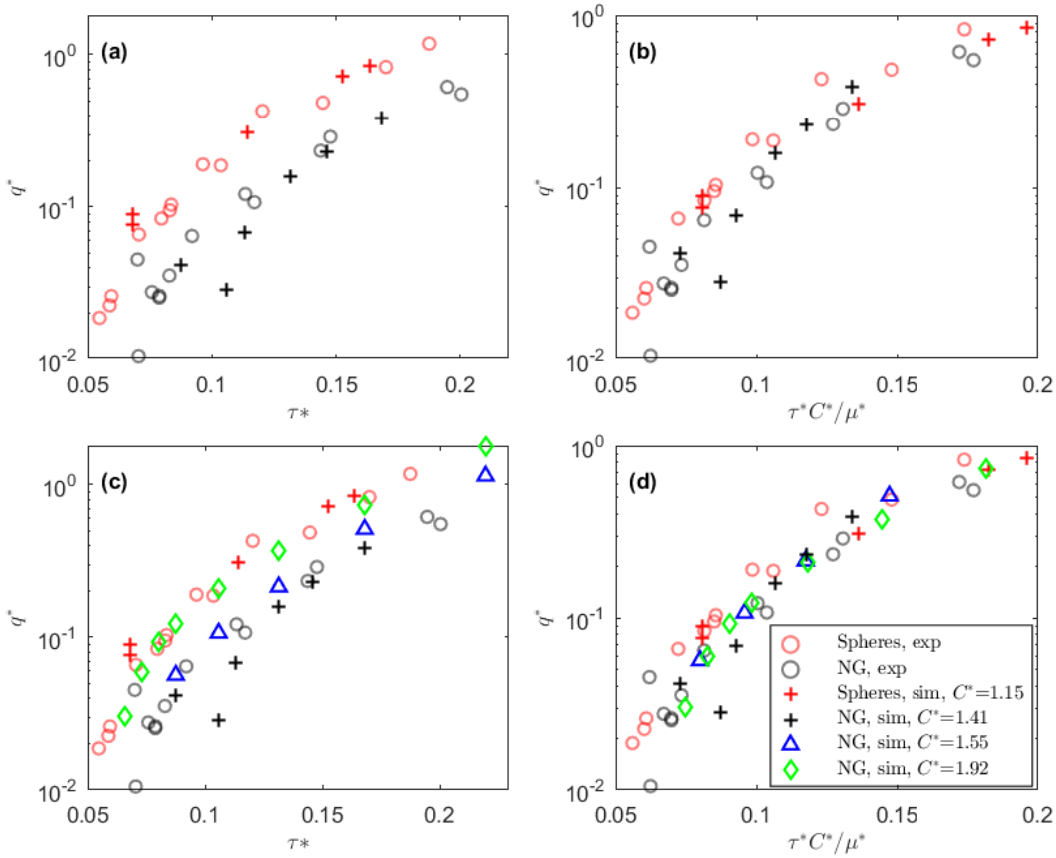

Figure 5: Dimensionless sediment transport rate q^* from DEM-LBM simulations of multi-sphere particles with (a, b) drag coefficients matching the settling experiments, and (c, d) various drag coefficients (by changing Sk). (a) & (c): Comparison with the q^* vs τ^* relation from experiments. (b) & (d): Comparison with the shape-corrected q^* vs $\tau^* C^*/\mu^*$ relation from experiments. The sediment transport relation data for experiments and simulations using spherical particles is also plotted in red for comparison. ("NG" means natural gravel.)

but different shrinkage coefficients $Sk = 0.55$ and $Sk = 0.00$ were carried out (corresponding to $C^* = 1.55$ and 1.92, see Table 3). The dimensionless transport relation is plotted in Figure 5(c). For the same set of multi-sphere particles, a larger value of Sk reduces the cross-sectional area and decreases the hydrodynamic force, leading to a higher threshold of motion and lower transport rate in general. Interestingly, the multi-sphere simulations with $Sk = 0.00$ give almost the same q^* vs τ^* relation as the glass spheres, even with a totally different combination of C^* and μ^* values. The modified sediment transport relation was also calculated using the average settling velocities for different Sk values, as shown in Figure 5(d). The collapse of the data points from the same set of particles with different drag coefficients confirms the robustness of Eq 5. It also relieves the concern that a shrinkage coefficient of $Sk = 0.70$ might be too big a change to the particle. Even with multi-spheres with smaller Sk values, as long as the average settling velocity of the particles is measured and taken into account, the modified sediment transport relation is able to collapse the data onto the master curve.

3.3 Particle orientation and other behaviors in the transport process

Recall that in Eq 5, C_D is calculated as the product of the drag coefficient of the particles settling in still water, $C_{D_{\text{settle}}}$, and the Corey shape factor, S_f, accounting for the fact that the orientation of the settling particle in still water prefers the largest drag while the orientation of the transported sediment particle is always changing due to rotation caused by the shear flow (no preferred orientation). There is a debate in previous numerical investigations on whether there is a preferred orientation of sediment particles when transported. B. Zhang et al. (2020) found that a single entrained particle keeps rotating without a preferred orientation. However, Jain et al. (2020) found that the transported particles tend to align with the bed surface. To quantify the alignment of the grains, we can look at the alignment between the bed (or downstream direction) and the primary axes of an aspherical particle. The latter can be determined by the minimum-volume bounding box as shown in Figure 6(a): the long axis with a unit vector $\boldsymbol{e_1}$, intermediate $\boldsymbol{e_2}$, and short $\boldsymbol{e_3}$. If the downstream and vertical directions are represented by unit vectors $\hat{\boldsymbol{x}}$ and $\hat{\boldsymbol{z}}$, then the probability density functions (PDFs) of inner-product $|\boldsymbol{e_3} \cdot \hat{\boldsymbol{z}}|$ and $|\boldsymbol{e_1} \cdot \hat{\boldsymbol{x}}|$ are both biased toward 1 according to Jain et al. (2020), suggesting the longest axis should be parallel to the downstream direction and the shortest axis perpendicular to the bed surface. The conflicting results from previous studies raise the question of whether there is any preferred orientation and how valid the quantification $C_D = C_{D_{\text{settle}}} S_f$ is in the sediment transport process. Observations in related situations give a hint. In dry circumstances (without considering the interaction between particles and fluid), aspherical particles aligns primarily with the bed under shear (Wang et al., 2020). There are also suggestions that the alignment statistics will depend on the distance the particles are from the bed. Indeed, in turbulent channels, (neutrally buoyant) spheroid particles (without particle-particle interactions) with large inertia rotate isotropically at the center of the channel while showing a preferred orientation near the wall (Zhao et al., 2015). Inspired by these observations, we hypothesize that in our case, the particles behave differently in different spatial regimes of the flow. Recently, Benavides et al. (2023) experimentally showed that the velocity distributions of the moving (spherical) particles are different near and farther from the bed surface in bedload transport. In this study, we are able to check the particle behaviors in terms of orientation with naturally shaped sediment particles.

Here, with the simulations designed to mimic the flume experiments, we carried out a statistical analysis of the particle orientation. The different spatial regimes of the flow were determined using a time-lapse of particle positions of 3000 snapshots during the last 30 s of the 40 s simulation, at a Shields number $\tau^* = 0.113$ (Figure 6b). The vertical coordinate, z, has its origin at the bed surface. The bed surface was calculated as the elevation of the highest stationary particle in the whole 30 s period, which moves less than $d_o/300$ in a sliding 1.5 s time window, similar to the previous work (Deal et al., 2023). According to their position, the particles can be divided into three regimes: the stationary particles deep in the bed, the dense flow near the bed surface with frequent contacts ($0 < z < 1.5d_o$), and the dilute flow regime ($z > 1.5d_o$). These three spatial regimes also corresponds to three different transport modes: creep below the bed surface, flows in traction, and saltation. The average flight time of the particles in the dilute regime is 0.17 s, corresponding to a mean rotation of 5.7 rotations per flight. Primary axes were examined on the particles not too close to the walls (at least 3 mm from the walls) during the same period, so that the alignment with walls in the bed and the boundary layers in the flow could be excluded. Here we quantified the alignment associated with two modes of particle motions. The first is the mode in which the particle is traveling with its largest cross-sectional area perpendicular to the flow, like the "sail on a ship". Figure 6(c) shows the probability distribution functions of $|\boldsymbol{e_3} \cdot \hat{\boldsymbol{x}}|$ in each of the three spatial regimes; a sail-like motion would have this inner-product be 1. These 3 PDF's for different regimes are almost flat (slightly biased towards 0), indicating the particle prefers not traveling with the largest cross-sectional area perpendicular to the

flow. The second is the mode in which the particle is moving like a "surf board," with its shortest axis perpendicular to the bed surface. Figure 6(d) shows the probability distribution functions of $|\boldsymbol{e_3}\cdot\hat{\boldsymbol{z}}|$. The PDF for the particles below the bed surface is strongly biased towards 1, indicating these particles prefer to align with the bed surface (e.g. a stacking of surf boards). Going further up, the PDF is less and less biased towards 1. Hence, the particles in the dilute regime show almost no preference for the alignment, since they are no longer in frequent contact with neighbors and can tumble freely. The PDF's of $|\boldsymbol{e_3}\cdot\hat{\boldsymbol{z}}|$ are similar to that observed in turbulent suspensions of neutrally buoyant spheroids (Zhao et al., 2015); their $|\boldsymbol{e_1}\cdot\hat{\boldsymbol{x}}|$ PDF looks similar to Figure 6(d) and $|\boldsymbol{e_1}\cdot\hat{\boldsymbol{z}}|$ has a PDF similar to Figure 6(c). Examination of the other 5 components of the primary axes show no biased distribution for the moving particles (dense and dilute flow) as well. In other words, the simulated grains tumble when in motion more and more freely as they go up farther and farther from the bed surface.

Our simulations at other Shields numbers also show similar particle behaviors: only $|\boldsymbol{e_3}\cdot\hat{\boldsymbol{z}}|$ and $|\boldsymbol{e_1}\cdot\hat{\boldsymbol{x}}|$ are biased towards 1 mostly for the dense flow regime, while all the other components of the primary axes for the dense regime and all components for the dilute regime are close to uniform distributions. Possible reasons for the strong bias observed in the previous work (Jain et al., 2020) are: (1) their particles had a low sphericity of 0.66, and (2) the particles all had identical size and shape, which made the particles more likely to show organized behaviors. For natural sediment particles whose shapes are distinct and whose sizes span a range, lower preferences of orientations may be expected, justifying the use of S_f in Eq 5. Sediment particles with extremely low sphericities such as shell fragments could show stronger orientational preferences. Our simulations also provide insights on other particle behaviors, for example, descending and ascending particles behave differently in terms of average velocity: the relative velocities between fluid and particles in the downstream direction are in general larger when particles are ascending. Correspondingly, ascending particles have larger downstream hydrodynamic drag forces than descending particles. See Text S2 in the Supporting Information for more details. These particle level physical observations are helpful for further theoretical developments on the transport threshold (Valyrakis et al., 2013; Pähtz et al., 2020) and the transport rate (Dey & Ali, 2017).

4 Concluding remarks

In this work, a complete workflow was developed for the numerical simulation of bedload sediment transport of naturally shaped particles, from particle shape measurement and approximation to fluid-coupled simulations of the aspherical particles. Superimposed spheres were used to approximate the shapes of naturally shaped gravel particles. In terms of the numerical method, sub-grain scale resolved DEM-LBM simulations of multi-sphere particles were implemented here for the first time. Our study attempts to closely match real experimental conditions. First, the most recent multi-sphere approximation algorithm was used to obtain more accurate shape representations. Second, many distinct realistic natural gravel shapes (more than 600 shapes) from CT scanning were represented in each simulation, permitting realistic size and shape distributions. Third, the numerical method was closely benchmarked with the corresponding flume experiments. The numerical method can also be applied to other geophysical problems related to fluid-particle mixture flows, such as subglacial till flows (Damsgaard et al., 2015) and crystal settling problems in magma chambers (Suckale et al., 2012).

In summation, sediment transport simulations of multi-sphere particles in the flume geometry were performed and results were compared with data from flume experiments. The simulations agree with the experimental repose angle of the dry material. The average settling velocity was calibrated with the experiments. The simulations were then shown to match the flume experiments in terms of the transport relation, bed structure, and collective behaviors of the particles. With validation in hand, the DEM-LBM tool

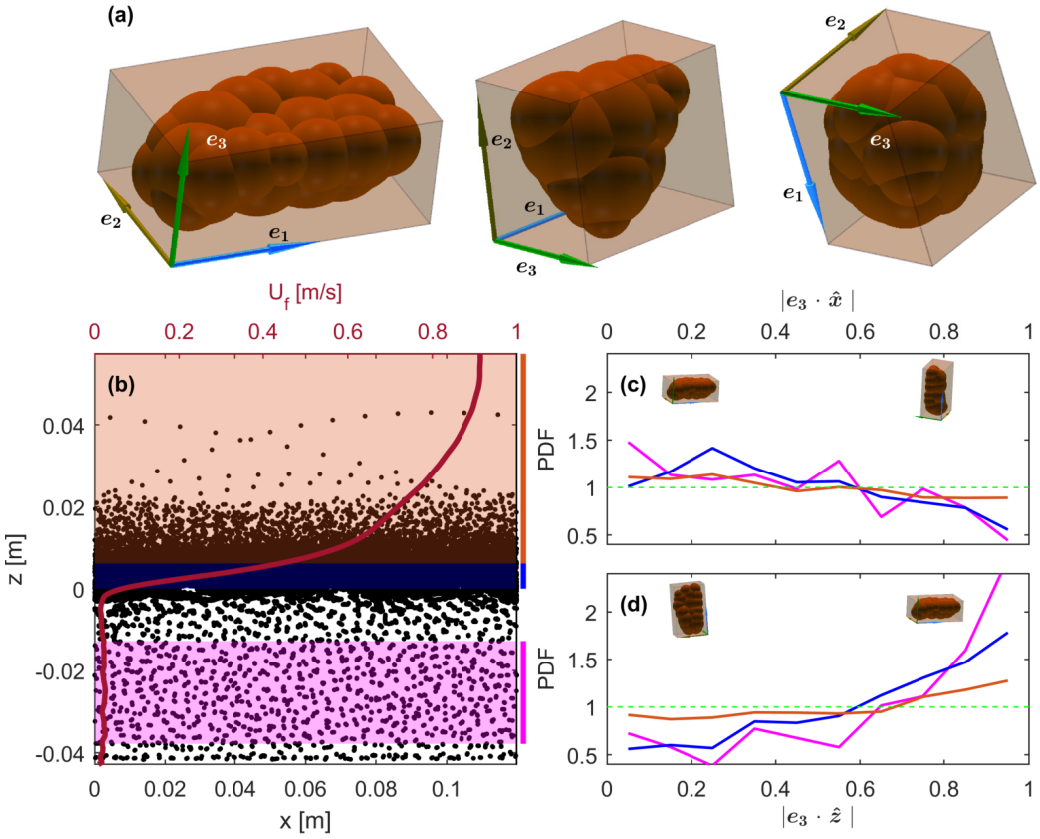

Figure 6: Particle orientation during the transport process. (a) Three examples of multi-sphere particles with the minimum bounding boxes and the primary axes: $\boldsymbol{e_1}$ long (cyan), $\boldsymbol{e_2}$ intermediate (yellow), and $\boldsymbol{e_3}$ short (green). (b) Time-lapse image of particle positions from the 10th second to the 40th second. The red line shows time-averaged fluid velocity in the flume as a function of elevation with respect to the bed surface, at Shields number $\tau^* = 0.113$. (c) & (d): Probability density function for the inner-product of $|\boldsymbol{e_3} \cdot \hat{\boldsymbol{x}}|$ (for values close to 1, traveling with the largest cross-sectional area perpendicular to the flow like a sail) and $|\boldsymbol{e_3} \cdot \hat{\boldsymbol{z}}|$ (for values close to 1, traveling like a surfing board). Four exemple orientations of the left particle in (a) are shown in (c) & (d), corresponding to the inner products. The 3 different colors correspond to the shaded areas in (b): Pink is the stationary bed, blue the dense particle flow near the bed surface, and orange the dilute flow. The green dashed lines are the uniform distribution.

was then used to demonstrate the robustness of a newly proposed shape-corrected sediment transport relation (Eq 5) by varying the drag coefficient while fixing all other grain properties via varying a shrinkage coefficient, Sk. These high resolution simulations also provide insights on the particle behaviors in the sediment transport process. Particles below the bed surface prefer to orient with their shortest axis perpendicular to the bed surface (like a surf board), but the tendency goes down as the packing fraction decreases far from the bed surface. The particles rotate freely in the dilute particle flow regime.

Open Research

The DEM-LBM solver and data are available via the following link: `https://figshare.com/articles/dataset/Data_for_Discrete_simulations_of_fluid-driven_transport_of_naturally_shaped_sediment_particles_/22647850` (Q. Zhang et al., 2023).

Acknowledgments

Research was sponsored by the Army Research Laboratory and was accomplished under Grant Number W911NF-16-1-0440. The views and conclusions contained in this document are those of the authors and should not be interpreted as representing the official policies, either expressed or implied, of the Army Research Laboratory or the U.S. Government. The U.S. Government is authorized to reproduce and distribute reprints for Government purposes notwithstanding any copyright notation herein.

References

Alihosseini, M., & Thamsen, P. U. (2018). Experimental and numerical investigation of sediment transport in sewers. In *Fluids engineering division summer meeting* (Vol. 51579, p. V003T17A005).

Allen, J. (2012). *Principles of physical sedimentology*. Springer Science & Business Media.

Amberger, S., Friedl, M., Goniva, C., Pirker, S., & Kloss, C. (2012). Approximation of objects by spheres for multisphere simulations in dem. *ECCOMAS-2012*.

Ardekani, M. N., Costa, P., Breugem, W.-P., Picano, F., & Brandt, L. (2017). Drag reduction in turbulent channel flow laden with finite-size oblate spheroids. *Journal of Fluid Mechanics*, *816*, 43–70.

Benavides, S. J., Deal, E., Rushlow, M., Venditti, J. G., Zhang, Q., Kamrin, K., & Perron, J. T. (2022). The impact of intermittency on bed load sediment transport. *Geophysical Research Letters*, e2021GL096088.

Benavides, S. J., Deal, E., Venditti, J. G., Bradley, R. W., Zhang, Q., Kamrin, K., & Perron, J. T. (2023). How fast or how many? sources of intermittent sediment transport. *Authorea Preprints*.

Blois, G., Best, J. L., Sambrook Smith, G. H., & Hardy, R. J. (2014). Effect of bed permeability and hyporheic flow on turbulent flow over bed forms. *Geophysical Research Letters*, *41*(18), 6435–6442.

Bouzidi, M., Firdaouss, M., & Lallemand, P. (2001). Momentum transfer of a boltzmann-lattice fluid with boundaries. *Physics of fluids*, *13*(11), 3452–3459.

Bravo, R., Ortiz, P., & Luis Pérez-Aparicio, J. (2018). Analytical and discrete solutions for the incipient motion of ellipsoidal sediment particles. *Journal of Hydraulic Research*, *56*(1), 29–43.

Corey, A. (1949). Influence of shape on fall velocity of sand grains [unpublished ms thesis]: Colorado a&m college. *Fort Collins, Colorado*.

Damsgaard, A., Egholm, D., Piotrowski, J., Tulaczyk, S., Larsen, N. K., & Bræstrup, C. (2015). A new methodology to simulate subglacial deformation of water-saturated granular material. *The Cryosphere*, *9*(6), 2183–2200.

Deal, E., Venditti, J. G., Benavides, S. J., Bradley, R., Zhang, Q., Kamrin, K., & Perron, J. T. (2023). Grain shape effects in bed load sediment transport. *Nature*, *613*(7943), 298–302.

Demir, T. (2000). *The influence of particle shape on bedload transport in coarse-bed river channels* (Unpublished doctoral dissertation). Durham University.

Derksen, J. J. (2014). Simulations of hindered settling of flocculating spherical particles. *International journal of multiphase flow*, *58*, 127–138.

Dey, S., & Ali, S. Z. (2017). Mechanics of sediment transport: Particle scale of entrainment to continuum scale of bedload flux. *Journal of Engineering Mechanics*, *143*(11), 04017127.

Donev, A., Cisse, I., Sachs, D., Variano, E. A., Stillinger, F. H., Connelly, R., ... Chaikin, P. M. (2004). Improving the density of jammed disordered packings using ellipsoids. *Science*, *303*(5660), 990–993.

Dudill, A., Venditti, J. G., Church, M., & Frey, P. (2020). Comparing the behaviour of spherical beads and natural grains in bedload mixtures. *Earth Surface Processes and Landforms*, *45*(4), 831–840.

Eshghinejadfard, A., Zhao, L., & Thévenin, D. (2018). Lattice boltzmann simulation of resolved oblate spheroids in wall turbulence. *Journal of Fluid Mechanics*, *849*, 510–540.

Favier, J., Abbaspour-Fard, M., & Kremmer, M. (2001). Modeling nonspherical particles using multisphere discrete elements. *Journal of Engineering Mechanics*, *127*(10), 971–977.

Favier, J., Abbaspour-Fard, M., Kremmer, M., & Raji, A. (1999). Shape representation of axi-symmetrical, non-spherical particles in discrete element simulation using multi-element model particles. *Engineering computations*.

Feng, Z.-G., & Michaelides, E. E. (2009). Robust treatment of no-slip boundary condition and velocity updating for the lattice-boltzmann simulation of particulate flows. *Computers & Fluids*, *38*(2), 370–381.

Ferguson, R., & Wathen, S. (1998). Tracer-pebble movement along a concave river profile: Virtual velocity in relation to grain size and shear stress. *Water Resources Research*, *34*(8), 2031–2038.

Fukuda, T., & Fukuoka, S. (2019). Interface-resolved large eddy simulations of hyperconcentrated flows using spheres and gravel particles. *Advances in Water Resources*, *129*, 297–310.

Fukuoka, S., Fukuda, T., & Uchida, T. (2014). Effects of sizes and shapes of gravel particles on sediment transports and bed variations in a numerical movable-bed channel. *Advances in water resources*, *72*, 84–96.

Jain, R., Tschisgale, S., & Froehlich, J. (2020). Effect of particle shape on bedload sediment transport in case of small particle loading. *Meccanica*, *55*(2), 299–315.

Jain, R., Tschisgale, S., & Fröhlich, J. (2021). Impact of shape: Dns of sediment transport with non-spherical particles. *Journal of Fluid Mechanics*, *916*.

Komar, P. D., & Li, Z. (1986). Pivoting analyses of the selective entrainment of sediments by shape and size with application to gravel threshold. *Sedimentology*, *33*(3), 425–436.

Li, C.-Q., Xu, W.-J., & Meng, Q.-S. (2015). Multi-sphere approximation of real particles for dem simulation based on a modified greedy heuristic algorithm. *Powder Technology*, *286*, 478–487.

Meyer-Peter, E., & Müller, R. (1948). Formulas for bed-load transport. In *Iahsr 2nd meeting, stockholm, appendix 2.*

Pähtz, T., Clark, A. H., Valyrakis, M., & Durán, O. (2020). The physics of sediment transport initiation, cessation, and entrainment across aeolian and fluvial environments. *Reviews of Geophysics*, *58*(1), e2019RG000679.

Rushlow, M. (2020). *Using machine learning, particle tracking, and grain shape modeling to characterize bedload sediment transport* (Bachelor's Thesis). Massachusetts Institute of Technology.

Schmeeckle, M. W. (2014). Numerical simulation of turbulence and sediment transport of medium sand. *Journal of Geophysical Research: Earth Surface*, *119*(6), 1240–1262.

Shao, B., Yan, Y., Yan, X., & Xu, Z. (2019). A study on non-spherical cuttings transport in cbm well drilling by coupled cfd-dem. *Engineering Applications of Computational Fluid Mechanics*, *13*(1), 579–590.

Shields, A. (1936). Application of similarity principles and turbulence research to bed-load movement.

Suckale, J., Sethian, J. A., Yu, J.-d., & Elkins-Tanton, L. T. (2012). Crystals stirred

up: 1. direct numerical simulations of crystal settling in nondilute magmatic suspensions. *Journal of Geophysical Research: Planets*, *117*(E8).

Sun, R., Xiao, H., & Sun, H. (2017). Realistic representation of grain shapes in cfd–dem simulations of sediment transport with a bonded-sphere approach. *Advances in water resources*, *107*, 421–438.

Swope, W. C., Andersen, H. C., Berens, P. H., & Wilson, K. R. (1982). A computer simulation method for the calculation of equilibrium constants for the formation of physical clusters of molecules: Application to small water clusters. *The Journal of chemical physics*, *76*(1), 637–649.

Valyrakis, M., Diplas, P., & Dancey, C. L. (2013). Entrainment of coarse particles in turbulent flows: An energy approach. *Journal of Geophysical Research: Earth Surface*, *118*(1), 42–53.

Wang, D., Zheng, H., Ji, Y., Barés, J., & Behringer, R. P. (2020). Shear of granular materials composed of ellipses. *Granular Matter*, *22*, 1–7.

Warburton, J., & Demir, T. (2000). Influence of bed material shape on sediment transport in gravel-bed rivers: a field experiment. In *Tracers in geomorphology* (pp. 401–410).

Yager, E. M., Schmeeckle, M. W., & Badoux, A. (2018). Resistance is not futile: Grain resistance controls on observed critical shields stress variations. *Journal of Geophysical Research: Earth Surface*, *123*(12), 3308–3322.

Zhang, B., Xu, D., Zhang, B., Ji, C., Munjiza, A., & Williams, J. (2020). Numerical investigation on the incipient motion of non-spherical sediment particles in bedload regime of open channel flows. *Computational Particle Mechanics*, *7*(5), 987–1003.

Zhang, Q., Deal, E., Perron, J. T., Venditti, J. G., Benavides, S. J., Rushlow, M., & Kamrin, K. (2022). Fluid-driven transport of round sediment particles: From discrete simulations to continuum modeling. *Journal of Geophysical Research: Earth Surface*, *127*(7), e2021JF006504.

Zhang, Q., Deal, E., Perron, J. T., Venditti, J. G., Benavides, S. J., Rushlow, M., & Kamrin, K. (2023). *Data for "discrete simulations of fluid-driven transport of naturally shaped sediment particles".* Retrieved from `https://figshare.com/articles/dataset/Data_for_Discrete_simulations_of_fluid-driven_transport_of_naturally_shaped_sediment_particles_/22647850` doi: 10.6084/m9.figshare.22647850.v1

Zhao, L., Challabotla, N. R., Andersson, H. I., & Variano, E. A. (2015). Rotation of nonspherical particles in turbulent channel flow. *Physical review letters*, *115*(24), 244501.

Zhong, W., Yu, A., Liu, X., Tong, Z., & Zhang, H. (2016). Dem/cfd-dem modelling of non-spherical particulate systems: theoretical developments and applications. *Powder technology*, *302*, 108–152.

Zhou, Z., Pinson, D., Zou, R., & Yu, A. (2011). Discrete particle simulation of gas fluidization of ellipsoidal particles. *Chemical Engineering Science*, *66*(23), 6128–6145.

Figure 5.

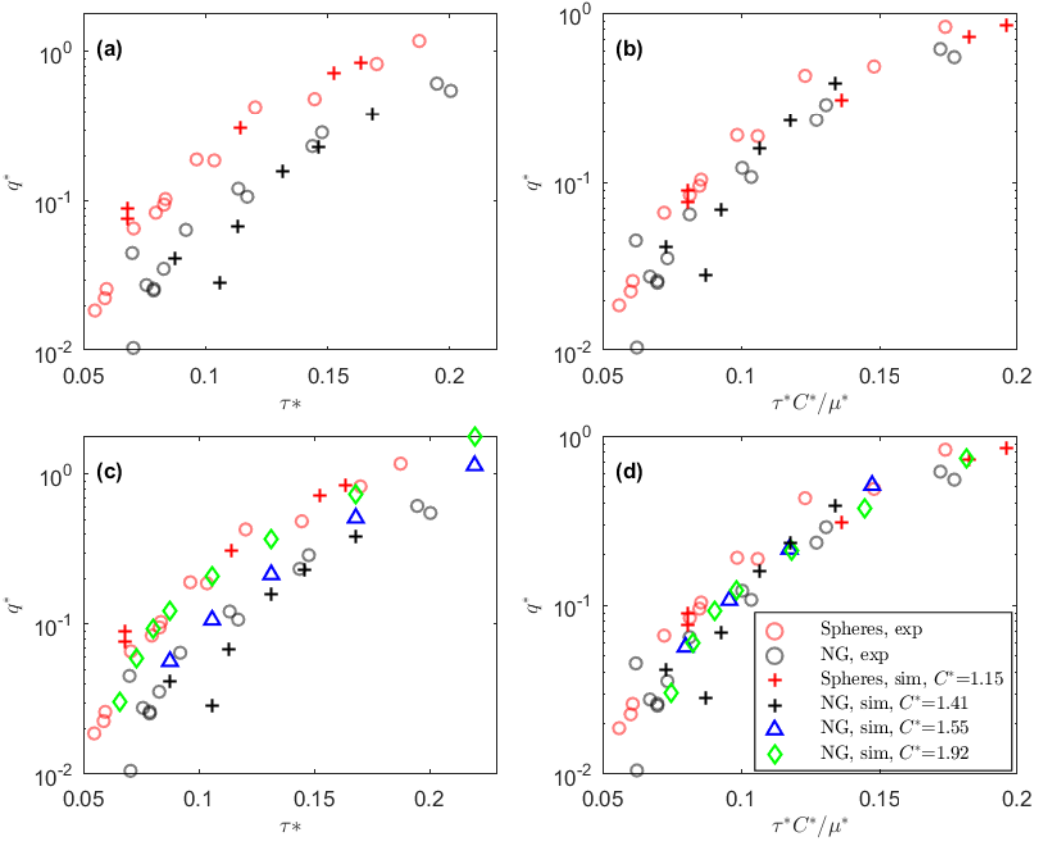
(a)
(b)
(c)
(d)
q^*
$\tau*$
$\tau^* C^*/\mu^*$
10^0
10^{-1}
10^{-2}
0.05
0.1
0.15
0.2
Spheres, exp
NG, exp
Spheres, sim, C^*=1.15
NG, sim, C^*=1.41
NG, sim, C^*=1.55
NG, sim, C^*=1.92

Figure 2.

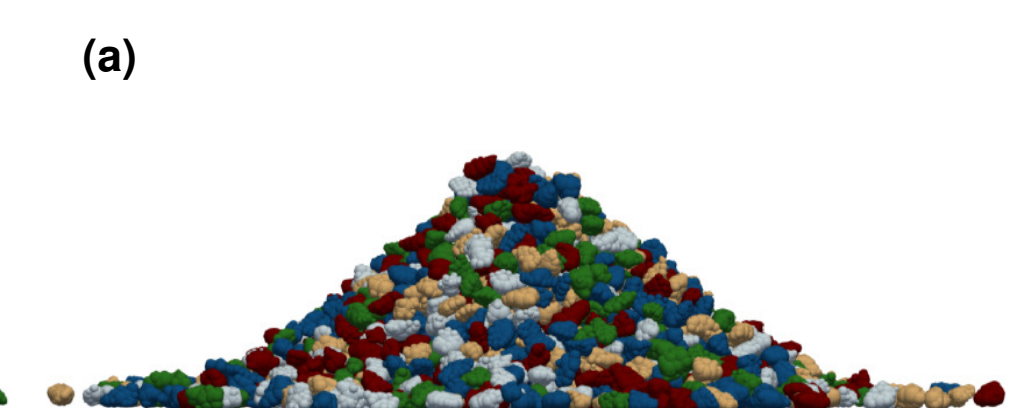
(a)

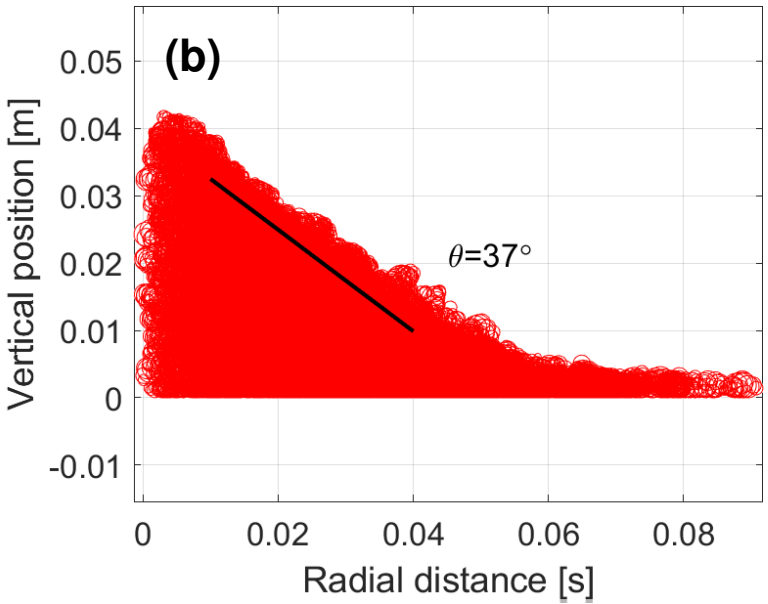
(b)
0.05
0.04
0.03
0.02
0.01
0
-0.01
Vertical position [m]
θ=37°
0
0.02
0.04
0.06
0.08
Radial distance [s]

Figure 1.

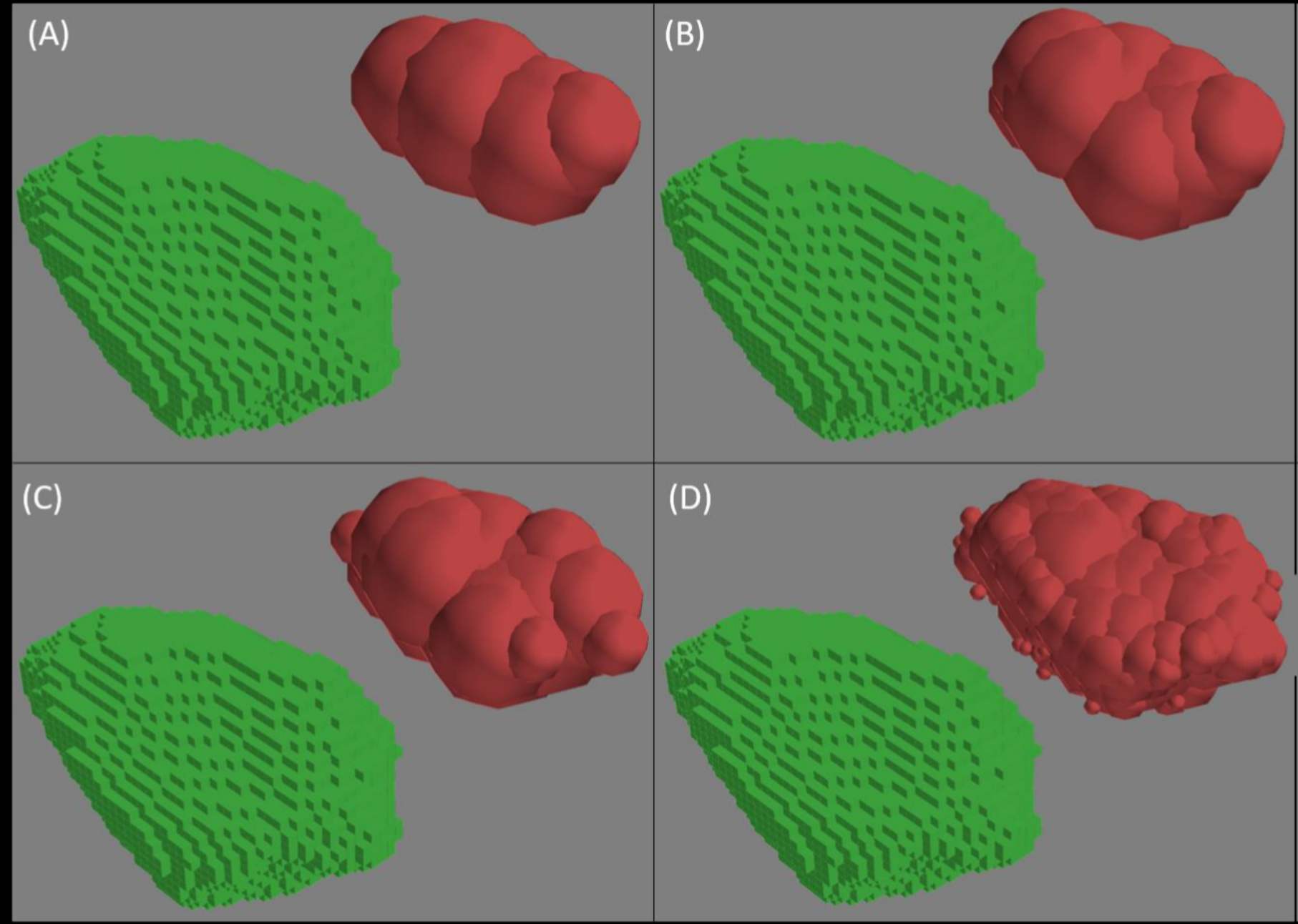
(A)
(B)
(C)
(D)

Figure 4.

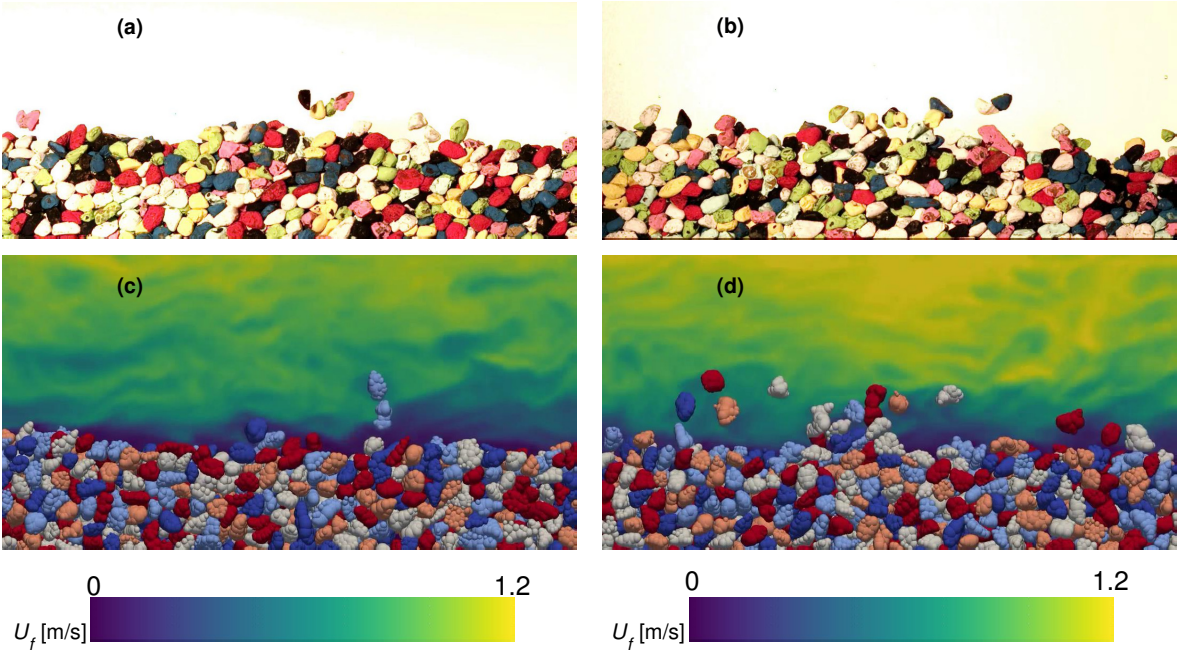
(a)
(b)
(c)
(d)
0
1.2
U_f [m/s]
0
1.2
U_f [m/s]

Figure 6.

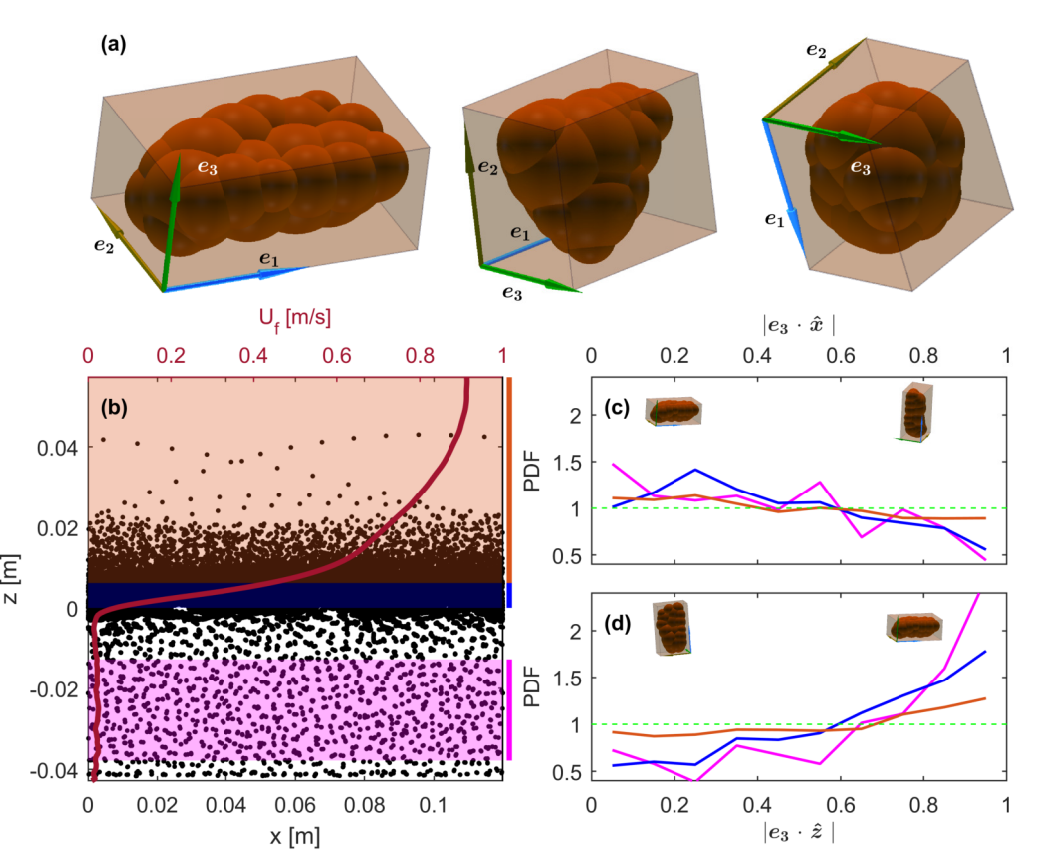
(a)
e_3
e_2
e_1
e_2
e_1
e_3
e_2
e_3
e_1
U_f [m/s]
$|e_3 \cdot \hat{x}|$
(b)
z [m]
x [m]
PDF
(c)
PDF
(d)
$|e_3 \cdot \hat{z}|$

Figure 3.

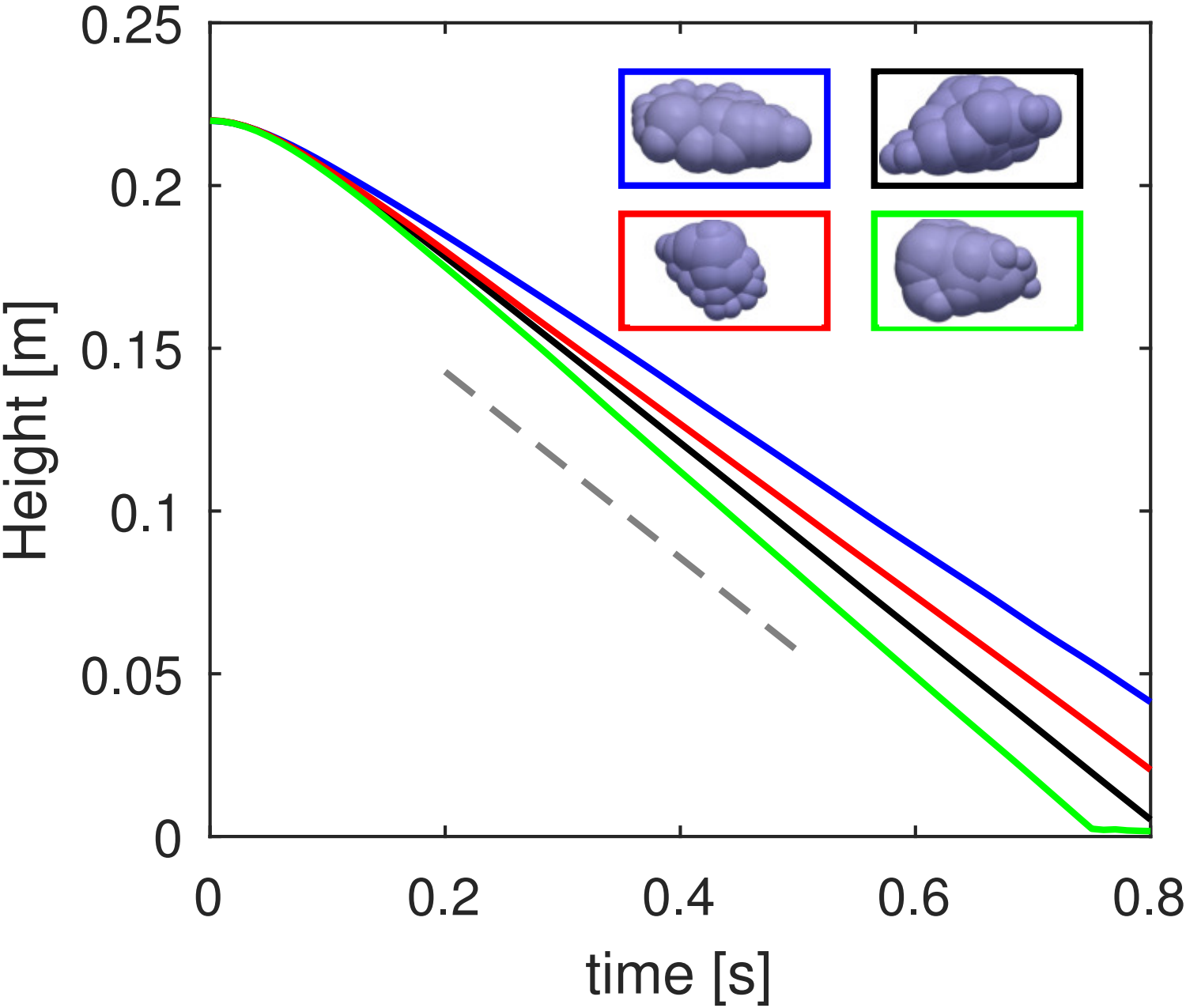
0.25
0.2
0.15
0.1
0.05
0
Height [m]
0
0.2
0.4
0.6
0.8
time [s]